Selective Reduction Laser Sintering
A New Strategy for NO_2 Gas Detection Based on In_2O_3 Nanoparticles

Wang, Shaogang; Tan, Chunjian; Zong, Qihang; Li, Shizhen; Gao, Chenshan; Yang, Huiru; Huang, Qianming; French, Paddy; Ye, Huaiyu

DOI
10.1002/adfm.202419057

Publication date
2025

Document Version
Final published version

Published in
Advanced Functional Materials

ADVANCED FUNCTIONAL MATERIALS
www.afm-journal.de

Selective Reduction Laser Sintering: A New Strategy for NO_2 Gas Detection Based on In_2O_3 Nanoparticles

Shaogang Wang, Chunjian Tan, Qihang Zong, Shizhen Li, Chenshan Gao, Huiru Yang, Qianming Huang, Paddy French, and Huaiyu Ye**

This study introduces a novel strategy for fabricating flexible nitrogen dioxide (NO_2) gas sensors based on Indium Oxide (In_2O_3) nanoparticles (NPs) employing selective reduction laser sintering (SRLS) technology. The SRSL technology utilizes ultraviolet (UV) laser selective reduction sintering to precisely and rapidly create oxygen vacancy (OV) defects in In_2O_3 NPs. These oxygen vacancies (OVs) enhance the active adsorption sites and contribute additional free electrons, significantly improving sensor performance at room temperature. The sensors demonstrate excellent response ($S = 460.9$ at 10 ppm), rapid response/recovery times ($\tau_{resp}/\tau_{reco} = 27/570$ s), and superior selectivity (response ratio > 400), in addition to robust resistance to light and humidity (under ppm-level NO_2 gas). The sensors also exhibit a low detection limit (200 ppb), a high signal-to-noise ratio (94.8 dB), and good long-term stability (25 days). Moreover, under photo-assisted conditions, the recovery speed of the sensors is further improved. This technology not only provides an innovative strategy for the development of high-performance flexible NO_2 gas sensors but also broadens the application potential of laser direct writing (LDW) technology in advanced materials and sensor fabrications.

1. Introduction

The rapid advancement of flexible sensors has surpassed the constraints of traditional sensors, becoming increasingly vital in both industrial production and daily life.[1] In addition to their applications in mechanical, thermoelectric, chemical, neuroelectric, and electrochemical signal processing, flexible sensors are increasingly emphasized for the precise and continuous detection of gas signals.[2] As environmental detection and health monitoring require increasingly higher accuracy and adaptability, flexible gas sensors have emerged as a focal point in sensor innovation.[3] Considering power consumption and operational safety, the development of room-temperature (RT) flexible gas sensors has become a significant trend, addressing both energy efficiency and operational reliability in complex environments.[4] Among the various gases, the detection of nitrogen dioxide (NO_2) has become especially critical, given its key role in environmental health monitoring (EHM). As a major by-product of fossil fuel combustion, NO_2 causes acid rain, photochemical smog, and ozone layer depletion, posing severe environmental risks.[5] Additionally, exposure to NO_2 at levels above the 3 ppm threshold is associated with severe health issues, including lung cancer, stroke, and asthma.[6] Therefore, the development of advanced RT flexible NO_2 sensors with excellent response, rapid response/recovery, and superior selectivity is an urgent priority.[7]

To enhance the performance of NO_2 gas sensors, researchers have explored various advanced materials such as metal oxide, conductive polymers, and carbon nanomaterials.[8] However, the synthesis of these materials typically involves energy-intensive, costly, and complex processes such as chemical vapor deposition, chemical polymerization, and arc discharge.[9] In addition, the fabrication of sensors based on these materials typically requires precisely engineered interdigitated electrodes made of precious metals such as platinum (Pt), gold (Au), and silver (Ag).[10] Indium Oxide (In_2O_3) stands out in applications such as solar cells, photocatalysis, and gas sensing due to its exceptional physical and chemical properties.[11] Notably, as an N-type semiconductor metal oxide, In_2O_3 exhibits high sensitivity and selectivity for detecting NO_2 gas.[12] To further enhance the performance of In_2O_3-based NO_2 sensors, nanomorphology controls such as nanofibers, nanosheets, and nanoparticles have been utilized to increase the surface activity of In_2O_3.[13] Additionally, functional modifications such as constructing heterostructures, nanocomposite, and defect engineering have been applied to enhance the electronic structures of In_2O_3.[14] Despite these advancements, In_2O_3-based gas sensors still face challenges such as limited gas selectivity, high operating temperature requirements, and

S. Wang, Q. Zong, S. Li, C. Gao, H. Yang, Q. Huang, H. Ye
School of Microelectronics
Southern University of Science and Technology (SUSTech)
Shenzhen 518055, P. R. China
E-mail: yehy@sustech.edu.cn
S. Wang, C. Tan, P. French, H. Ye
Faculty of EEMCS
Delft University of Technology (TU Delft)
Mekelweg 4, Delft 2628 CD, The Netherlands
E-mail: p.j.french@tudelft.nl

The ORCID identification number(s) for the author(s) of this article can be found under https://doi.org/10.1002/adfm.202419057

DOI: 10.1002/adfm.202419057

performance degradation under humid conditions, which restrict their broader application.[15]

In response to these challenges, laser direct writing (LDW) technology has revolutionized the fabrication of flexible gas sensors with its excellent processing accuracy and control capability.[16] This technology utilizes a laser beam to precisely remove, add, or modify both the surface and interior of target materials, achieving high-resolution heat treatments at the micron or submicron level.[17] Selective laser sintering (SLS), a subset of LDW technology, is widely used for the sintering and modifying of metal, ceramic, and metal oxide nanoparticles, attributed to its low heat input and high thermal gradient.[18] Meanwhile, this technology allows maskless and customized rapid sintering processes on various substrates controlled by computer software.[19] Defect engineering, an effective material modification method, plays a crucial role in optimizing the properties of sensor materials.[20] Specifically, laser-induced defect engineering has made significant breakthroughs in enhancing gas sensor performance. This technique introduces beneficial oxygen vacancies, opening new pathways to improve the detection capability of the sensor significantly. For In_2O_3 nanoparticles, the introduction of oxygen vacancy (OV) defects not only increases the number of adsorption sites but also modulates the electronic structure, which significantly improves the sensitivity and selectivity of the sensor.[21] However, the efficient fabrication of In_2O_3 NPs with OV defects for flexible NO_2 gas sensing using SLS technology continues to pose a significant challenge.

In this study, we report the development of the flexible NO_2 gas sensor using selective reduction laser sintering (SRLS) technology. This technology selectively reduces polyvinyl pyrrolidone (PVP) coated In_2O_3 nanoparticles (NPs) by controlling the key parameters of a UV pulse laser, thereby enabling the formation of OV defects in In_2O_3 NPs. Owing to the introduction of oxygen vacancies (OVs), the sensors demonstrate excellent response (S = 460.9 at 10 ppm), rapid response/recovery (τ_{resp}/τ_{reco} = 27/570 s), and superior selectivity (response ratio > 400) at RT (25 °C). Furthermore, the sensors exhibit robust resistance to light and humidity and an even faster recovery speed under photo-assisted conditions. The sensors also demonstrate a low detection limit (200 ppb), a high signal-to-noise ratio (94.8 dB), and good long-term stability, maintaining reliable performance for up to 25 days. Through experimental verification and material characterization, the impact of varying laser scanning intervals on the OV defects and sensing performance was further explored. Additionally, the adsorption mechanism of the NO_2 molecule on In_2O_3 with OV was investigated through theoretical calculations. This technology not only provides a new strategy for the fabrication of flexible NO_2 sensors based on In_2O_3 with OVs but also further expands the application prospects of LDW technology in material science and device fabrication.

2. Results and Discussion

2.1. Investigation of the SRLS Process

Unlike traditional selective laser sintering (SLS), where the laser is directly applied to the material surface to achieve high-temperature solid-phase transformation, selective reduction laser sintering (SRLS) achieves nanoparticle sintering by finely adjusting the temperature distribution at the edges of the laser scanning path. The fabrication of the flexible gas sensors using this technology consists of four main steps: blade coating, laser sintering, surface cleaning, and electron printing (**Figure 1a**). The detailed methodology of this fabrication process is described in the Supporting Information (Experimental Section). In the most critical laser sintering process, In_2O_3 NPs serve as both a crucial material for flexible gas sensors and as an essential coating for triggering the photothermal effect. It is well known that polyethylene terephthalate (PET) has a relatively low absorption coefficient for UV lasers. Therefore, when the laser is vertically irradiated onto PET films, most of the laser energy passes through without causing any noticeable physical or chemical reaction.[22] However, when the PET surface is coated with In_2O_3 NPs, the In_2O_3 layer absorbs UV laser energy and rapidly converts it into thermal energy. This conversion triggers a significant pyrolysis reaction on the shallow surface of PET through the photothermal effect. Under UV irradiation, the high energy density of the laser leads to the ablation of the In_2O_3 layer and the underlying PET substrate, forming a laser-ablated region. At the same time, the high temperature generated by the laser-ablated region causes the unirradiated In_2O_3 NPs to undergo rapid thermal sintering at the edge of the laser scanning path, forming a distinct laser-sintered region. In contrast, regions that have not been ablated and sintered can be easily removed by deionized water cleaning (Figure 1b).

The composition of In_2O_3 nanoparticle (NP) paste, primarily consisting of active and carrier materials, is crucial for the formation of OV defects during the SRLS process. Detailed explanations of the active material and the carrier material are provided in the (Section S1, Supporting Information). Building on this, the thermal properties of In_2O_3 NP paste and its carrier were analyzed using thermogravimetric/derivative thermogravimetric (TG/DTG) and differential scanning calorimetry (DSC) to investigate the formation mechanism of OV defects. After comparative analysis, the thermal weight loss of In_2O_3 NP paste at a low heating rate (10 °C min^{-1}) was summarized into three main stages (Figure S4, Supporting Information). The process initiates with the evaporation of organic solvents within the temperature range of 30–170 °C. This is followed by the decomposition of polyvinylpyrrolidone (PVP) side chains, occurring between 170–300 °C. The final stage involves the critical breakdown of the PVP backbone, which occurs from 300–550 °C. In the final stage, reduced macromolecules generated by the decomposition of the PVP main chain partially reduce In_2O_3 to metallic Indium (In) while forming OV defects.[23] This provides a specific reference for further understanding the mechanism of the SRLS with a high-temperature gradient. Detailed analyses of the TG/DTG and DSC are presented in the (Section S2, Supporting Information).

To explore the effects of various laser parameters on the SRLS process, a series of experimental optimizations were performed using a UV laser system (Figure S7, Supporting Information). The experiments focused on finely tuning key parameters such as laser scanning speed (V_{ss}), average laser power (P_{avg}), pulse repetition frequency (F_{pr}), and defocus distance (D_{def}), all of which are closely related to the sensor performance and fabrication efficiency. Given the importance of both magnitude and stability

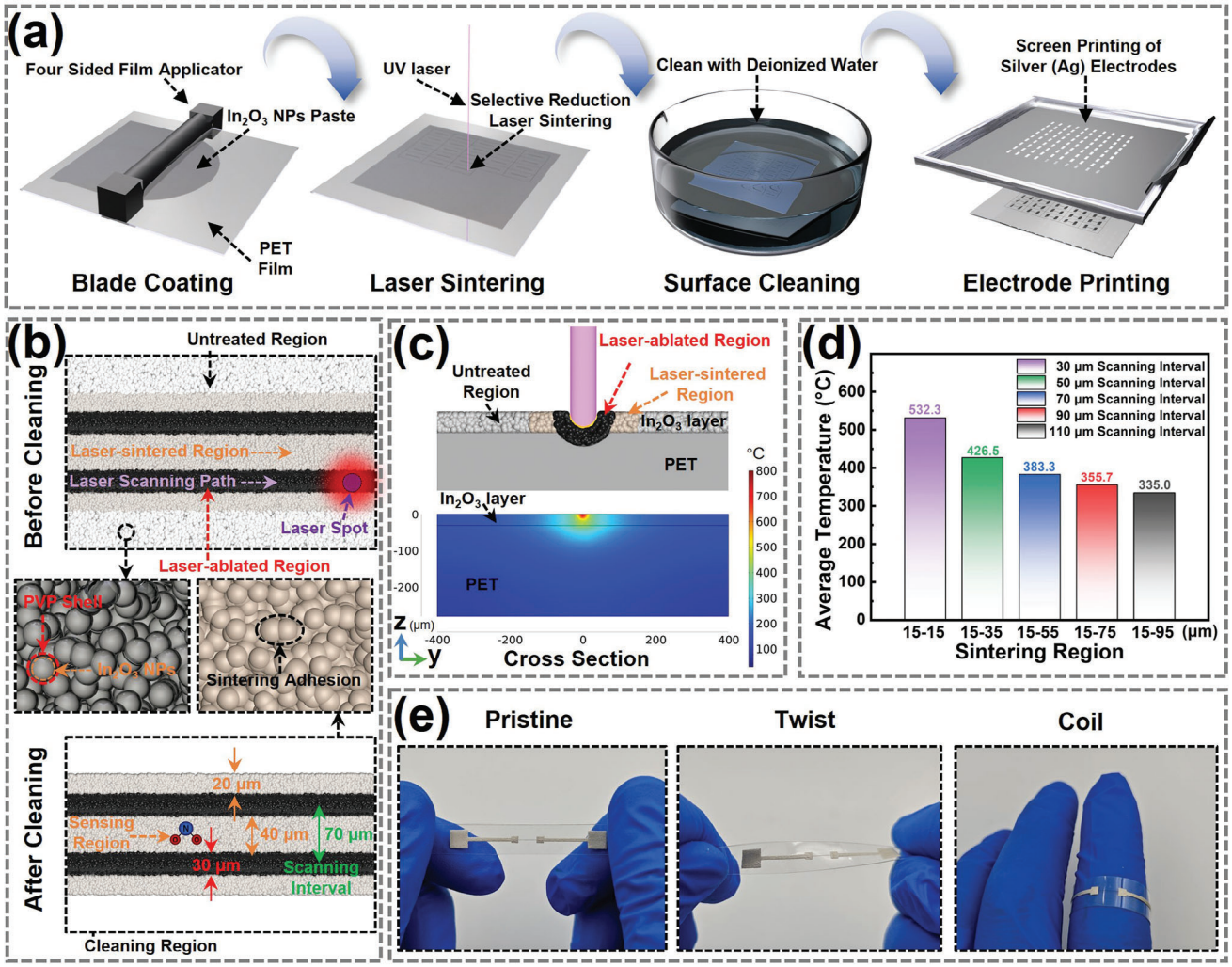

Figure 1. The fabrication process for flexible NO_2 gas sensors is based on the SRLS technology. a) Schematic diagram of the sensor fabrication process. b) Schematic illustration of the structural changes on the surface of In_2O_3 NPs due to laser sintering. c) Schematic structure and temperature distribution of the sensor cross-section during laser sintering. d) Histogram of equivalent average sintering temperatures for laser-sintered regions with different scanning intervals. e) Demonstration of the sensor in different deformation states.

in the initial resistance of the sensing region, the optimal laser parameters were set to 10 mm s^{-1} for V_{ss}, 0.27 W for P_{avg}, 200 kHz for F_{pr}, and 0 mm for D_{def} (Figure S10, Supporting Information). Detailed parameter optimization and implementation of the SRLS process are provided in (Section S3 and Video S1, Supporting Information).

To achieve OV defect control, the critical sintering temperature in the SRLS process is precisely controlled by the laser scanning interval. However, the high energy density and rapid scanning speed of UV lasers present significant challenges in monitoring the real-time temperature during the SRLS process. To further calibrate the influence of the laser scanning interval on the sintering temperature, finite element analysis (FEA) was used to simulate the temperature distribution and evolution within the In_2O_3 layer and PET substrate during the single laser scanning process. The cross-sectional temperature distribution at the midpoint of the linear laser scanning reveals that the photothermal effect of the laser generates a high-temperature region exceeding 800 °C at the top center of the model, with a sharp decrease in temperature along the *y*- and *z*-axes (Figure 1c). This temperature distribution radiates outward from the center of the heat source, forming a high-temperature region and temperature diffusion regions on either side of it, corresponding to the laser ablation and laser-sintered regions (70 μm scanning interval). The equivalent average temperatures of the laser-sintered region on one side of the laser scanning are 523.3, 426.5, 383.3, 355.7, and 335.0 °C at various scanning intervals, with corresponding effective sintering close intervals of 15–15 μm, 15–35 μm, 15–55 μm, 15–75 μm, and 15–95 μm (Figure 1d). Detailed simulation model construction and discussion of the temperature distribution and evolution during linear laser scanning are provided in (Section S4, Supporting Information).

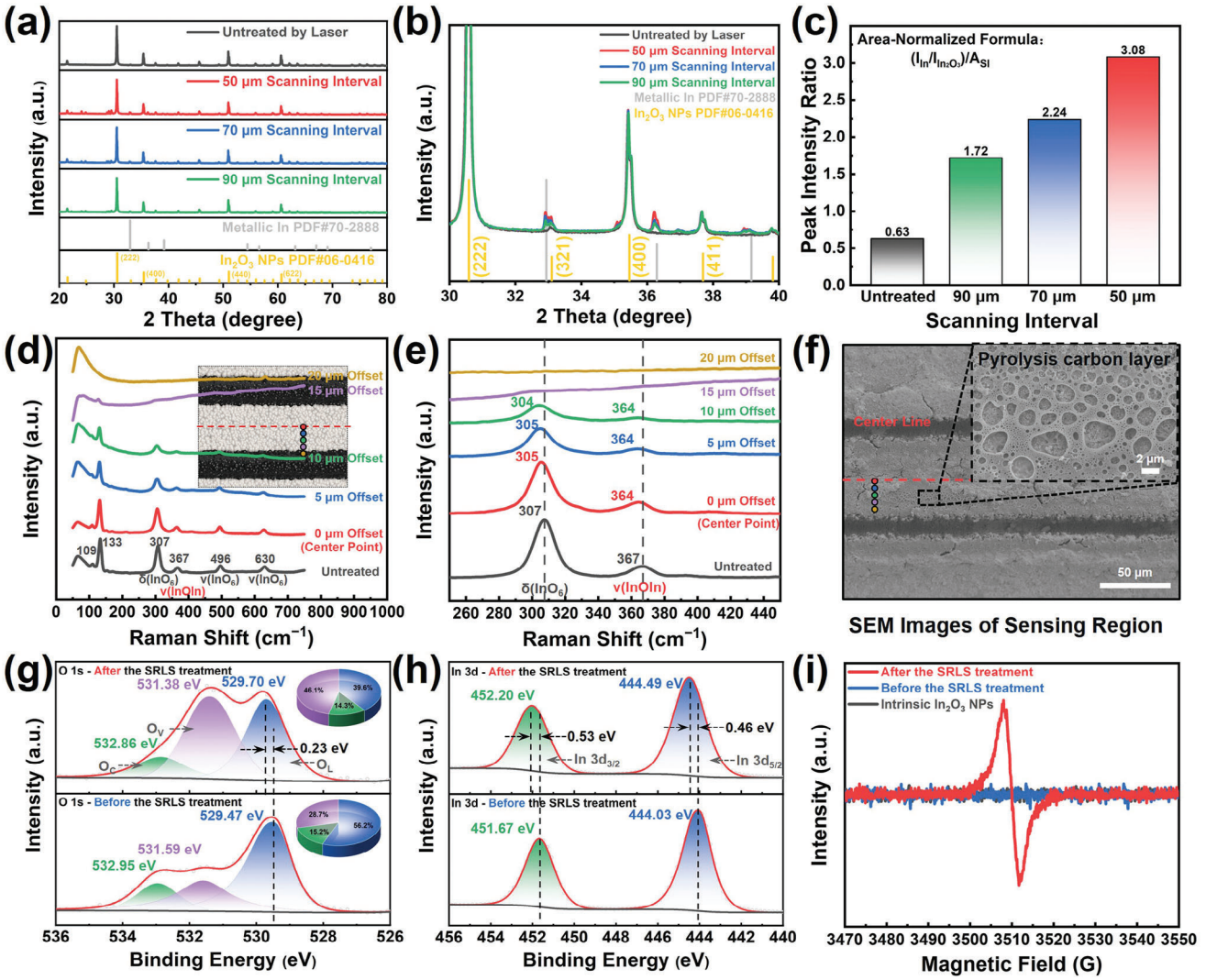

Figure 2. Characterization of OV defects in In_2O_3 NPs. a) Overall and b) local XRD patterns of In_2O_3 before and after the SRLS treatment. c) Ratio of area-normalized peak intensities in In_2O_3 XRD patterns at different laser scanning intervals. d) Overall and e) local Raman spectra of In_2O_3 at different points within the laser-sintered region. f) SEM images of the laser-sintered region. g) O 1s and h) In 3d XPS spectra of In_2O_3 before and after the SRLS treatment. i) EPR spectra of In_2O_3 before and after the SRLS treatment.

Benefiting from the high energy density and rapid scanning speed of the laser, the SRLS technology offers more flexible customization while significantly reducing the temperature requirements of the substrate material. This technology enables the rapid fabrication of flexible gas sensors on 250 μm thick PET films, ensuring excellent sensing performance while maintaining stable mechanical properties (Figure 1e).

2.2. Characterization of OV Defects

To investigate the effect of different laser scanning intervals on the crystal structure and phase transition of In_2O_3 NPs in the SRLS treatment, X-ray diffraction (XRD) patterns were employed to characterize the samples with untreated, 50, 70, and 90 μm scanning intervals (**Figure** 2a). The XRD pattern of untreated In_2O_3 NPs indicates characteristic peaks at 30.6°, 35.5°, 51.0°, and 60.7°, corresponding to the (222), (400), (440), and (622) crystal planes (PDF#06-0416). However, the SRLS-treated In_2O_3 NPs (including both the laser-ablated and laser-sintered regions) exhibit both peaks for In_2O_3 as well as new peaks for metallic In at 32.9°, 36.3°, 39.2°, and 54.4° (PDF#70-2888). The transition from In_2O_3 to metallic In is clearly evident from the comparison of the overall peak intensities in the XRD spectra. It is noteworthy that the intensities of the metallic In peaks near the (321) and (400) crystal planes increase significantly with decreasing laser scanning intervals in the diffraction angle range from 30° to 40° (Figure 2b). In addition, normalization of the effective area of the laser scanning region shows that the intensity ratio of diffraction peaks of metal In to In_2O_3 near the (321) crystal plane increases significantly with decreasing scanning intervals (Figure 2c). These results indicate that the transformation

of In_2O_3 to metallic In during the SRLS process is further promoted by the increase in sintering temperature with the decrease in laser scanning interval. Furthermore, local XRD patterns reveal that the diffraction peaks near the (321) crystal plane of In_2O_3 shift to a lower 2θ angle as the sintering temperature increases due to a decrease in the scanning interval (Figure S17, Supporting Information).[24] This shift indicates an expansion of the interplanar spacing in the In_2O_3 crystal, leading to a relaxation of the lattice structure.[25] Notably, this also indicates that Indium ions in In_2O_3 have been reduced to lower valence or even metallic states, implying the generation of OV defects.[26] Detailed discussions and localized XRD spectra of the In_2O_3 NP paste before and after SLRS treatment are provided in (Section S5.1, Supporting Information).

To analyze the structure and composition of In_2O_3 NPs after the SRLS treatment (70 µm scanning interval), Raman spectroscopy was employed to characterize different points within the sensing region on the side perpendicular to the scanning direction (Figure 2d). Raman spectra were collected at five points spaced 5 µm apart from the center of the sensing region within the wavelength range of 50–750 cm^{-1} (Figure S21, Supporting Information). For comparison, the Raman spectra of pure In_2O_3, PVP, and PET are presented in (Figures S22, Supporting Information). Besides the ultra-low frequency peak at 66 cm^{-1} from PET substrates, untreated In2O3 NPs exhibit six prominent peaks at 109, 133, 307, 367, 496, and 630 cm^{-1}, providing insights into the vibrational modes and properties of In_2O_3.[27] In the lower frequency range, the lattice vibrational peaks at 109 and 133 cm^{-1} indicate large-scale motions involving the In atoms or the entire lattice structure.[28] The peak at 307 cm^{-1} correlates with the symmetric bending vibrations of $\delta(InO_6)$ octahedra.[29] Similarly, the peaks at 496 and 630 cm^{-1} are associated with asymmetric stretching vibrations of $\nu(InO_6)$ octahedra.[26]

Notably, the 367 cm^{-1} scattering feature, identified as ν(InOIn) stretching vibrations, indicates the presence of OV defects in the In_2O_3 lattice.[24,30] After the SRLS treatment, the Raman spectra of In_2O_3 show a slight redshift in characteristic peaks, indicating the formation of OV defects. These defects lead to the expansion and local relaxation of the In_2O_3 lattice structure and the weakening of the In—O bond. Consequently, the reduced bonding strength alters the vibrational mode of the In—O—In bridge, resulting in a shift of the Raman peak to a lower wavelength (Figure 2e).[31] Furthermore, Raman spectra collected at 0, 5, and 10 µm offset points show a gradual decrease in overall relative peak intensity closer to the laser scanning region. Even more, the Raman spectra of the 15 and 20 µm offset points show significant anomaly. Scanning electron microscopy (SEM) characterization reveals that the PET substrate is slightly melted in the laser scanning region due to the photothermal effect (Figure 2f). The sputtering of molten PET onto In_2O_3 NPs near the laser-ablated region formed a porous pyrolytic carbon layer, which interferes with Raman spectra analysis.[32] Detailed analyses of Raman spectra, SEM, and energy dispersive X-ray (EDX) of the laser-sintered region are provided in (Section S5.2, Supporting Information). This provides a certain reference for further understanding the mechanism of the SRLS.

To further determine the chemical composition and defect state of the In_2O_3 NPs before and after the SRLS process (70 µm scanning interval), the sensing region was analyzed by X-ray photoelectron spectroscopy (XPS). The full XPS survey reveals significant changes in the intensity of the binding energy peaks of In, O, and C elements before and after the SRLS treatment (Figure S25, Supporting Information). After the SRLS treatment, the intensities of the In 3d and O 1s peaks decreased significantly. In comparison, the intensity of the C 1s peak increased, demonstrating the formation of pyrolytic carbon on the surface of the laser-sintered region. Furthermore, before the SRLS treatment, the O1s peaks at 529.47, 531.59, and 532.95 eV correspond to different oxygen species in In_2O_3 NPs: lattice oxygen (O_L), oxygen vacancy (O_V), and chemisorbed oxygen (O_C), respectively (Figure 2g).[24,33] After the SRLS treatment, the O_L peak shifts to 529.70 eV, a positive shift of 0.23 eV. This shift indicates electronic interactions between polyvinylpyrrolidone (PVP) and In_2O_3, suggesting that the pyrolysis products of PVP contribute to the reduction and removal of lattice oxygen from In_2O_3, thereby reducing the average oxidation state in the O 1s peak.[34] Specifically, the relative peak area ratio of O_L decreases from 56.2% to 39.6%, reflecting a decrease of 16.6%. Conversely, the O_V peak area ratio increases from 28.7% to 46.1%, representing a significant increase of 17.4% (pie chart in Figure 2g). This directly demonstrates a significant increase in the density of OV defects after the SRLS treatment.[26] Furthermore, compared to the sensing region before the SRLS treatment, the In $3d_{5/2}$ and $3d_{3/2}$ XPS peaks of the In_2O_3 exhibit positive shifts of 0.46 and 0.53 eV, respectively (Figure 2h). This suggests electron transfer from In_2O_3 to pyrolytic carbon in the PVP pyrolysis product, thus dispersing electron density around In atoms.[31]

Additionally, the electron spin resonance (EPR) results reveal that the In_2O_3 NPs after the SRLS treatment exhibit a signal at a g-value of 2.03, which suggests that the electrons are trapped in the OV defects generated by the reduction of In_2O_3 by pyrolysis products during the SRLS process (Figure 2i). This result further confirms the presence of OV defects in In_2O_3 after the SRLS treatment.[35] The methodology and process for calculating the g-value are introduced in (Section S5.4, Supporting Information).

2.3. Testing of Sensor Performance

Variations in sintering temperature due to different laser scanning intervals (30, 50, 70, 90, and 110 µm) significantly affect the performance of N-type chemoresistive gas sensors based on In_2O_3 NPs during the SRLS process. To evaluate this effect, the sensor was exposed to a specific NO_2 gas concentration for 30 s at RT (Figure S29, Supporting Information). The relative response of the gas sensor is quantified as $S = \Delta R/R_0 = (R-R_0)/R_0$, where R and R_0 represent the stabilized resistance in the target gas and air environments, respectively. The response (τ_{resp}) and recovery (τ_{reco}) times are defined as the times required to achieve a 90% change in resistance when exposed to NO_2 and air.[36] Detailed descriptions of the sensing test platform and test procedure are provided in (Section S6.1, Supporting Information). Test results show that sensor resistance spikes sharply when exposed to 10 ppm NO_2 and then gradually recovers in the air. Interestingly, as the sintering temperature increases with decreasing laser scanning interval, the sensor response to NO_2 decreases significantly with values of 967.62, 802.16, 442.24, 19.69, and 18.27,

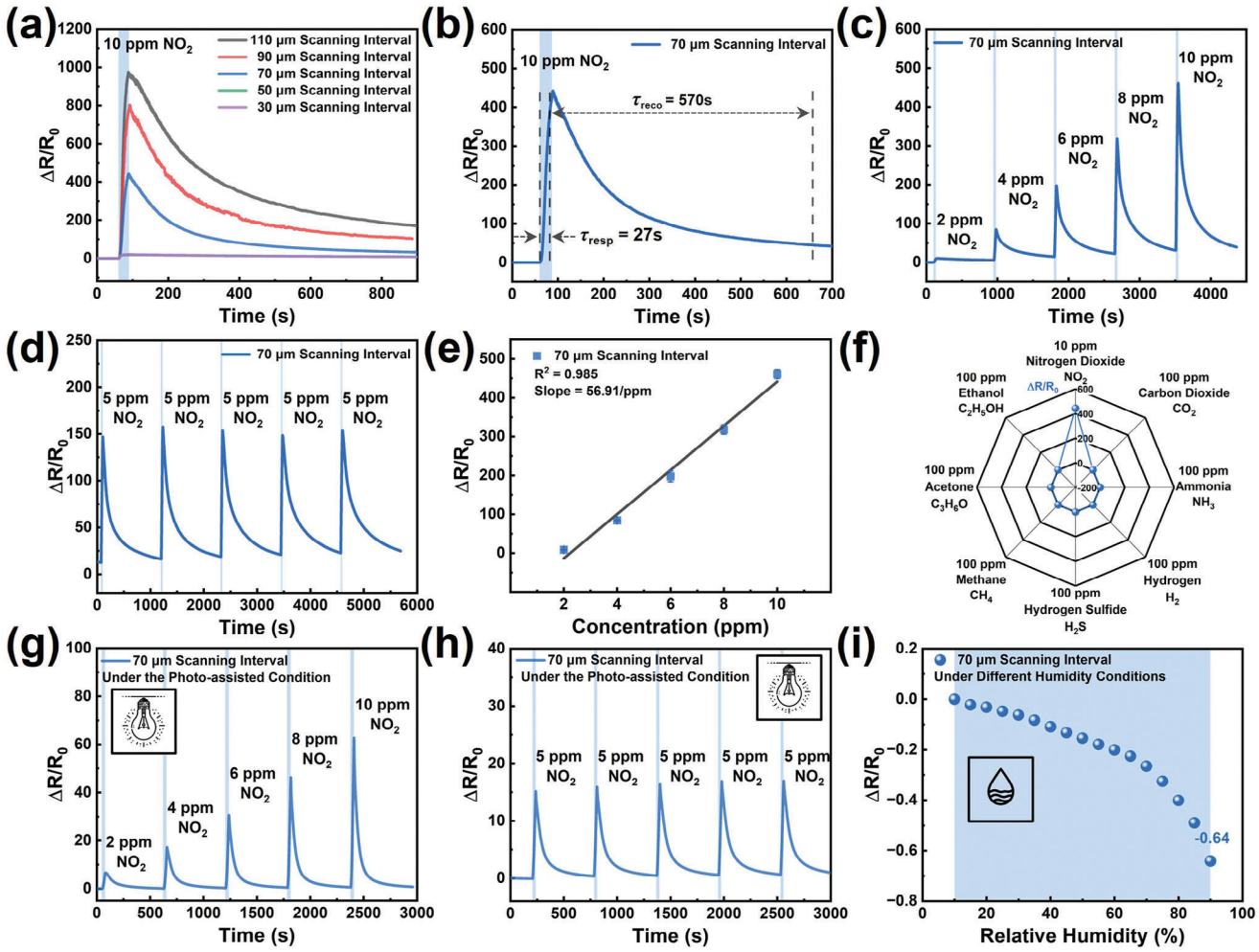

Figure 3. Performance testing of sensors based on SRLS technology. a) Response curves of the sensor to 10 ppm NO_2 with different scanning intervals. b) Typical response curve of the sensor. c) Dynamic response curve of the sensor to NO_2 from 2 to 10 ppm. d) Repeatability response curve of the sensor to 5 ppm NO_2 over five consecutive cycles. e) Linear fit curve of the sensor response to NO_2 from 2 to 10 ppm with error bars representing three samples. f) Radar chart of the sensor selectivity for NO_2 compared to other interfering gases. g) Dynamic response curve of the sensor to NO_2 from 2 to 10 ppm under the photo-assisted condition. h) Repeatability response curve of the sensor to 5 ppm NO_2 over five consecutive cycles under the photo-assisted condition. i) Sensor response curve for relative humidity ranging from 10% to 90%.

respectively (**Figure 3a**). Higher sintering temperatures lead to an increase in OV defects, which theoretically should enhance the ability of NO_2 to capture electrons within the sensing region, thereby promoting a significant increase in sensor resistance change (ΔR).[37] However, narrower scanning intervals increase the baseline resistance (R_0) of the sensor (Figures S31 and S32), Supporting Information. Consequently, the sensing gain from the increase in OV defects is counteracted by the increase in baseline resistance, which significantly reduces the sensor response to NO_2. On the other hand, a larger scanning interval enlarges the effective adsorption area of the sensor, offering more sites for adsorption but also extending the desorption time, which slows down the recovery ability of the sensor.[38] Additionally, the lower sintering temperature associated with an increased scanning interval reduces the adhesion between the In_2O_3 NP layer and the PET substrate, challenging the stability and reliability of the sensor.[39] To balance performance and stability, the sensor with a 70 μm scanning interval was selected for further evaluation.

The sensor exhibits rapid response and recovery times of 27 and 570 s for 10 ppm NO_2 at RT (Figure 3b). Additionally, the sensor also consistently detects 5 ppm NO_2 over five cycles, demonstrating high repeatability and reversibility (Figure 3c). Furthermore, as NO_2 concentrations increase from 2 to 10 ppm, the sensor response gradually increases from 9.8 to 460.9, indicating excellent dynamic response capabilities (Figure 3d). Correspondingly, the linear response of the sensor for NO_2 concentrations ranging from 2 to 10 ppm exhibits a slope of 56.91 ppm^{-1} and an R^2 of 0.985, demonstrating stable linear response characteristics (Figure 3e). Notably, the response of the sensor to 10 ppm NO_2 (response ratio > 400) is significantly stronger than its response to 100 ppm of the interfering gases (C_2H_5OH, CO_2, C_3H_6O, NH_3, CH_4, and H_2S), proving its superior selectivity (Figure 3f). Moreover, the signal-to-noise ratio (SNR) for the response curve to

10 ppm NO_2 is 94.8 dB (Figure S33, Supporting Information). The corresponding SNR calculation and analysis are shown in (Section S6.2, Supporting Information). The detection limit (LOD) of the sensor is as low as 200 ppb, with a response rate of 0.426 (Figure S34, Supporting Information). The sensor demonstrates long-term stability, with a response deviation of less than 10% over 25 days (Figure S35, Supporting Information). Correspondingly, the mechanical reliability test and analysis of the sensor are further introduced in (Section S6.3, Supporting Information).

Considering the practical application of the sensor, the impact of environmental factors such as light and humidity on the sensor performance was further evaluated. Unsurprisingly, flexible gas sensors based on In_2O_3 NPs with OV defects demonstrate excellent NO_2 gas detection performance along with inherent optoelectronic properties.[37] Under the photo-assisted condition (xenon lamp irradiation), the resistance of the sensor decreases due to light-induced electronic excitation. This excitation promotes the transition of electrons from the valence band to the conduction band, leading to the formation of additional electron–hole pairs and enhancing the electrical conductivity of the sensor.[40] Additionally, OV defects in In_2O_3 serve as trapping centers for electrons or holes, stabilizing and extending the lifetimes of photogenerated carriers. This trapping effect reduces the electron–hole recombination rate, further reducing the resistance of the sensor.[41] Under the photon-assisted condition, the sensor demonstrates excellent consistency and reversibility in response to five consecutive 5 ppm NO_2 at RT (Figure 3g). Meanwhile, the photon-assisted response of the sensor gradually increased from 6.6 to 62.7 as the concentration of NO_2 increased from 2 to 10 ppm, demonstrating its robust dynamic response and recovery under bright light (Figure 3h). Importantly, although photon assistance significantly reduces the response of the sensor to NO_2, the photon-assisted sensing mechanism enhanced the half-recovery speed by 91.7% in low NO_2 concentration detection (Figure S38, Supporting Information). These properties not only demonstrate the light resistance of the sensor but also further expand its application potential in continuous NO_2 sensing applications. Considering the inherent sensitivity of semiconductor materials to humidity, the response of the sensor to different relative humidity (RH) conditions was further evaluated (Figure 3i).[42] The results indicate that as relative humidity increases, the relative resistance of the sensor decreases. At high humidity levels (90% RH), the response to humidity measures only −0.64. Although the impact of humidity on the sensor can generally be neglected when detecting high concentrations of NO_2 (under ppm levels), significant limitations appear when detecting low concentrations of NO_2 (under ppb levels). Correspondingly, in (Section S6.4, Supporting Information), the testing and analysis of the sensor under lighting and humidity conditions are further discussed, illustrating its potential applicability and challenges in practical applications.

Compared with gas based on In_2O_3 and other advanced materials, the sensors fabricated using SRLS technology offer enhanced flexibility, efficiency, and high customizability, along with superior compatibility and adaptability. In terms of performance, these sensors demonstrate excellent sensitivity to NO_2, rapid response and recovery times, and superior selectivity. In addition, these sensors exhibit a low detection limit, high signal-to-noise ratio, and good long-term stability (Table S1, Supporting Information). A detailed comparison of the sensor performance is discussed in (Section S6.5, Supporting Information).

2.4. Analysis of Sensing Mechanism

The primary sensing mechanism of NO_2 gas sensors based on In_2O_3 NPs fabricated by SRLS technology is driven by conductivity changes resulting from the adsorption and desorption of gas molecules on the sensor surface. Specifically, the OVs on the surface of In_2O_3 NPs play a crucial role in facilitating this mechanism. These defects enable electrons to transition from the valence band to the conduction band, thereby increasing the concentration of free electrons and enhancing the conductivity of the sensing region.[43] Concurrently, these defects offer active adsorption sites in the sensing region, thereby increasing the adsorption of oxygen species.[44]

When the sensor is exposed to an air atmosphere, the oxygen (O_2) molecules adsorb onto the surface of In_2O_3 NPs and capture free electrons from the conduction band to form O_2^-(ads) ions with higher chemical activity, as detailed in reaction Equations (1) and (2).[45]

$$O_2\,(\text{gas}) \leftrightarrow O_2\,(\text{ads}) \tag{1}$$

$$O_2\,(\text{ads}) + e^- \rightarrow O_{2^-}\,(\text{ads}) \tag{2}$$

This reaction process depletes the carrier concentration on the surface of In_2O_3, causing the energy bands to bend upward and forming a surface electron depletion layer (**Figure 4a**). When the sensor is exposed to a NO_2 gas atmosphere, the NO_2 molecules interact directly with the electrons in the conduction band of In_2O_3 to form NO_2^-(ads) ions, driven by their high electron affinity.[46] Additionally, these NO_2 molecules can also react with pre-existing O_2^-(ads) ions to form NO_3^- ions, as described in the reaction Equations (3) and (4).[45]

$$NO_2\,(\text{ads}) + e^- \rightarrow NO_{2^-}\,(\text{ads}) \tag{3}$$

$$O_{2^-}\,(\text{ads}) + 2NO_2\,(\text{ads}) \rightarrow 2NO_{3^-}\,(\text{ads}) \tag{4}$$

This reaction process further deepens the electron depletion layer on the In_2O_3 surface, which enhances the upward bending of the energy bands and significantly increases the resistance of the In_2O_3 NPs. Furthermore, both of these processes deplete the conduction band electrons in In_2O_3 NPs, resulting in an increased thickness of the electron depletion layer and an elevated potential barrier energy. However, due to its strong oxidizing properties, NO_2 tends to play a dominant role in the reactions at RT, which significantly increases the resistance of the sensor and enables the detection of NO_2 gas.[47]

To further investigate the adsorption mechanism of NO_2 molecules on In_2O_3 and the role of OVs in enhancing this process, we performed a detailed computational analysis using density functional theory (DFT). Specifically, based on the number of O atoms bonded to In atoms in the In_2O_3 unit cell and the coordination numbers of these O atoms, 16 different adsorption sites (Figures S41 and S42, Supporting Information) are

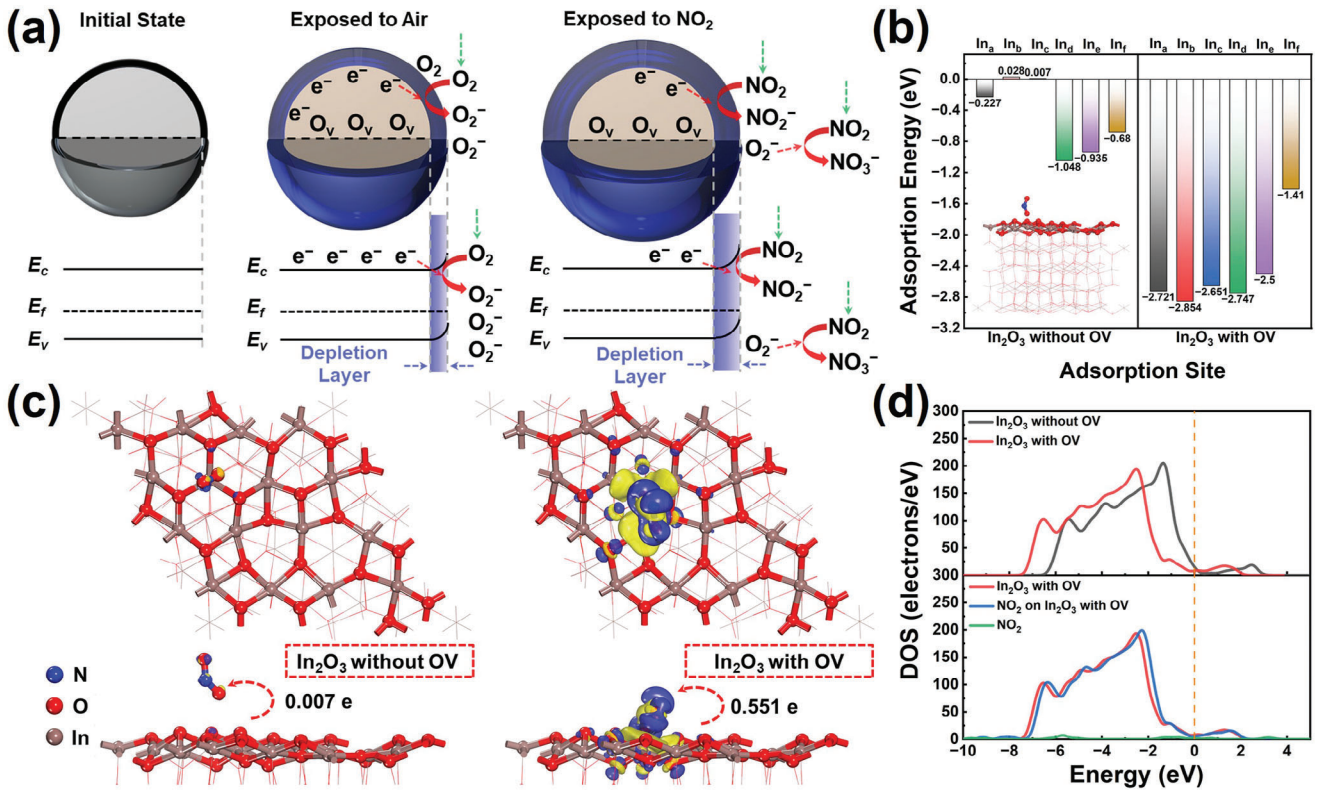

Figure 4. Senning mechanisms of NO_2 on In_2O_3 sensors with OV defects. a) Schematic diagram of the sensing mechanism. b) Histograms of adsorption energy in different adsorption systems and different adsorption modes. c) CDD distributions of In_2O_3 with and with OV after NO_2 adsorption (The isosurface is set as 0.01 e $Å^{-3}$. The blue region indicates electron accumulation and the yellow region represents electron depletion. d) DOS curves of In_2O_3 with and without OV, and DOS curves of In_2O_3 with OV before and after NO_2 adsorption.

classified into 6 distinct adsorption modes (Table S2, Supporting Information). Compared to In_2O_3 without OV, In_2O_3 with OV shows a stronger adsorption reaction to NO_2 molecules at various adsorption modes (Figure 4b). In particular, the presence of OV at the In_{22} site in the In_b adsorption mode significantly enhances its adsorption capacity. This enhancement is thoroughly compared and analyzed using charge density difference (CDD) and density of states (DOS) calculations. The CDD results show that the interaction of the NO_2 molecule in the In_2O_3 adsorption system without OV not only causes a slight electron accumulation of O atoms on the In_2O_3 surface but also leads to a subtle charge rearrangement inside the NO_2 molecule (Figure 4c). In this process, NO_2 acts as an electron acceptor, receiving 0.07 e from the In_2O_3 as determined by Mulliken charge analysis.[48] The corresponding adsorption energy of 0.028 eV indicates that the reaction in this adsorption mode (In_b) is not spontaneous (Table S3, Supporting Information). This positive adsorption energy further demonstrates the limitations of intrinsic In_2O_3 in adsorbing NO_2 molecules.[49] Conversely, in the In_2O_3 adsorption system with OV, the CDD results reveal a more intense electronic interaction induced by the adsorption of the NO_2 molecule on the In_2O_3 surface. Specifically, the adsorption of the NO_2 molecule leads to the formation of large-volume electron depletion regions between it and three neighboring In atoms of In_2O_3. Additionally, the N and O atoms of NO_2 exhibit distinct electron accumulation regions, while an overall electron depletion region is demonstrated around the N—O bonds. In this process, the NO_2 serves as an electron acceptor, receiving 0.551 e from the In_2O_3, which indicates the formation of chemical solid adsorption between the NO_2 and the In_2O_3 with OV.[50] Moreover, the corresponding adsorption energy of −2.854 eV confirms that the adsorption process is exothermic, indicating its spontaneous nature and highlighting a clear contrast with intrinsic In_2O_3 (Table S4, Supporting Information).

By comparing the DOS curves of In_2O_3 with and without OV, it is clear that the introduction of OV shifts the DOS curve toward lower energy levels and flattens the curves near the Fermi level (Figure 4d). This shift indicates that the introduction of the defect state creates localized states within the band gap of In_2O_3, which increases the density of electronic states and introduces intermediate energy levels.[51] This enhancement not only reduces the energy required for electron excitation from the valence to the conduction band but also provides additional electrons and transition pathways.[52] Furthermore, when the NO_2 molecule is adsorbed on the surface of In_2O_3 with OV, the DOS curve for the corresponding system shifts slightly to higher energy, and the density of electronic states near the Fermi level decreases. This change confirms that NO_2 adsorption promotes electron transfer from the In_2O_3 surface to the NO_2 molecule, resulting in charge redistribution and rearrangement of energy levels.[53] Overall, these results clearly demonstrate the substantial potential of OV in improving the sensitivity of NO_2 gas sensors

based on In_2O_3 NPs fabricated by SRLS technology and provide a solid theoretical basis for understanding the sensing mechanism. The classification of different adsorption modes, the corresponding adsorption sites, adsorption energies, adsorption distances, and charge transfer are discussed in (Section S7, Supporting Information).

3. Conclusion

In summary, we have successfully developed a selective reduction laser sintering (SRLS) technology based on In_2O_3 NPs to fabricate flexible NO_2 sensors efficiently. This technology employs a UV laser to selectively reduce PVP-coated In_2O_3 NPs spin-coated on PET substrates to prepare In_2O_3 sensing regions with oxygen vacancy (OV) defects. OV defects significantly increase the active adsorption sites, thereby enhancing the capture rate of NO_2. This also introduces additional free electrons, subsequently improving the conductivity of the sensor. Due to the advantages offered by these properties, In_2O_3 NPs with OV defects exhibit outstanding NO_2 sensor performance at room temperature. The sensors not only exhibit exceptional response values ($S = 460.9$ at 10 ppm), rapid response/recovery ($\tau_{resp}/\tau_{reco} = 27/570$ s), and superior selectivity (response ratio > 400) but also demonstrate robust resistance to light and humidity under ppm-level NO_2 conditions. The sensors further feature a low detection limit (200 ppb), a high signal-to-noise ratio (94.8 dB), and good long-term stability (25 days). Additionally, the recovery speed of the sensors can be further enhanced under the photo-assisted condition. This work proposes a new strategy for developing high-performance flexible NO_2 sensors. It provides key insights into the mechanism of NO_2 adsorption by In_2O_3 NPs with OVs, paving the way for the development of flexible gas sensors for environmental health monitoring.

Supporting Information

Supporting Information is available from the Wiley Online Library or from the author.

Acknowledgements

This work was supported by the Guangdong Basic and Applied Basic Research Foundation (2023B1515120090) and the Shenzhen Major Science and Technology Projects (KJZD20230923114710022).

Conflict of Interest

The authors declare no conflict of interest.

Data Availability Statement

The data that support the findings of this study are available from the corresponding author upon reasonable request.

Keywords

flexible gas sensor, indium oxide nanoparticles, nitrogen dioxide, oxygen vacancy defect, selective reduction laser sintering

Received: October 9, 2024
Revised: January 16, 2025
Published online:

[1] a) A. Sharma, M. Z. Ansari, C. Cho, *Sens. Actuators, A.* **2022**, *347*, 113934; b) Q. Li, L. N. Zhang, X. M. Tao, X. Ding, *Adv. Healthcare Mater.* **2017**, *6*, 1601371; c) S. S. Aaryashree, P. Walke, S. K. Nayak, C. S. Rout, D. J. Late, *Nano Res.* **2021**, *14*, 3669; d) Y. Cho, S. Park, J. Lee, K. J. Yu, *Adv. Mater.* **2021**, *33*, 2005786; e) F. Gao, C. Liu, L. Zhang, T. Liu, Z. Wang, Z. Song, H. Cai, Z. Fang, J. Chen, J. Wang, *Microsyst. Nanoeng.* **2023**, *9*, 1.

[2] M. Javaid, A. Haleem, S. Rab, R. P. Singh, R. Suman, *Sens. Int.* **2021**, *2*, 100121.

[3] a) S. D. Lawaniya, S. Kumar, Y. Yu, H.-G. Rubahn, Y. K. Mishra, K. Awasthi, *Mater. Today Chem.* **2023**, *29*, 101428; b) H. R. Ansari, A. Mirzaei, H. Shokrollahi, R. Kumar, J.-Y. Kim, H. W. Kim, M. Kumar, S. S. Kim, *J. Mater. Chem. C.* **2023**, *11*, 6528; c) L.-X. Ou, M.-Y. Liu, L.-Y. Zhu, D. W. Zhang, H.-L. Lu, *Nano-Micro Lett.* **2022**, *14*, 206.

[4] Y. Cheng, B. Ren, K. Xu, I. Jeerapan, H. Chen, Z. Li, J. Z. Ou, *J. Mater. Chem. C.* **2021**, *9*, 3026.

[5] a) B. Rani, U. Singh, A. Chuhan, D. Sharma, R. Maheshwari, *J. Adv. Sci. Res.* **2011**, *2*, 28; b) M. T. Lerdau, J. W. Munger, D. J. Jacob, *Science* **2000**, *289*, 2291.

[6] a) K. Wetchakun, T. Samerjai, N. Tamaekong, C. Liewhiran, C. Siriwong, V. Kruefu, A. Wisitsoraat, A. Tuantranont, S. Phanichphant, *Sens. Actuators, B.* **2011**, *160*, 580; b) S. Edginton, D. E. O'Sullivan, W. D. King, M. D. Lougheed, *Environ. Res.* **2021**, *192*, 110296; c) N. Yi, M. Shen, D. Erdely, H. Cheng, *TrAC, Trends Anal. Chem.* **2020**, *133*, 116085.

[7] a) X. Liu, H. Zhang, T. Shen, J. Sun, *Ceram. Int.* **2024**, *50*, 2459; b) C.-R. Yang, J.-G. Huang, M.-J. Huang, H.-Y. Shen, S.-F. Tseng, *J. Alloys Compd.* **2024**, *1008*, 176675; c) Y. Men, Z. Qin, Z. Yang, P. Zhang, M. Li, Q. Wang, D. Zeng, X. Yin, H. Ji, *Adv. Funct. Mater.* **2024**, *34*, 2316633; d) W. Wei, N. Luo, X. Wang, Z. Xue, L. A. Shah, Q. Hu, J. Xu, *Sens. Actuators, B.* **2024**, *414*, 135944; e) W. Quan, J. Shi, M. Zeng, B. Li, Z. Liu, W. Lv, C. Fan, J. Wu, X. Liu, J. Yang, *ACS Sens.* **2024**, *9*, 4578.

[8] a) Y. Wu, N. Joshi, S. Zhao, H. Long, L. Zhou, G. Ma, B. Peng, O. N. Oliveira Jr, A. Zettl, L. Lin, *Appl. Surf. Sci.* **2020**, *529*, 147110; b) Y. Sun, Y. Zhang, *Chem. Eng. J.* **2023**, *473*, 145480; c) B. L.e Ouay, M. Boudot, T. Kitao, T. Yanagida, S. Kitagawa, T. Uemura, *J. Am. Chem. Soc.* **2016**, *138*, 10088.

[9] a) Y. Seekaew, D. Phokharatkul, A. Wisitsoraat, C. Wongchoosuk, *Appl. Surf. Sci.* **2017**, *404*, 357; b) X. Yan, Z. Han, Y. Yang, B. Tay, *Sens. Actuators, B.* **2007**, *123*, 107; c) C. T. Xuan, C. M. Hung, N. Van Duy, T. M. Ngoc, Q. T. M. Nguyet, N. D. Hoa, *Adv. Nat. Sci. Nanosci. Nanotechnol.* **2022**, *13*, 035007.

[10] a) H. Liu, M. Li, O. Voznyy, L. Hu, Q. Fu, D. Zhou, Z. Xia, E. H. Sargent, J. Tang, *Adv. Mater.* **2014**, *26*, 2718; b) T. Stockinger, D. Wirthl, G. Mao, M. Drack, R. Pruckner, S. Demchyshyn, M. Steiner, F. Egger, U. Müller, R. Schwödiauer, *Adv. Mater.* **2021**, *33*, 2102736; c) X. Cao, Y. Xiong, J. Sun, X. Zhu, Q. Sun, Z. L. Wang, *Adv. Funct. Mater.* **2021**, *31*, 2102983.

[11] a) P. Chen, X. Yin, M. Que, Y. Yang, X. Liu, W. Que, *J. Alloys Compd.* **2018**, *735*, 938; b) P. Chang, Y. Wang, Y. Wang, Y. Zhu, *Chem. Eng. J.* **2022**, *450*, 137804; c) T. Waitz, T. Wagner, T. Sauerwald, C. D. Kohl, M. Tiemann, *Adv. Funct. Mater.* **2009**, *19*, 653.

[12] S. Shah, S. Hussain, S. T. U. Din, A. Shahid, J. N. O. Amu-Darko, M. Wang, Y. Tianyan, G. Liu, G. Qiao, *J. Environ. Chem. Eng.* **2024**, *12*, 112538.

[13] a) F. Gu, C. Li, D. Han, Z. Wang, *ACS Appl. Mater. Interfaces* **2018**, *10*, 933; b) L. Sun, W. Fang, Y. Yang, H. Yu, T. Wang, X. Dong, G. Liu, J.

Wang, W. Yu, K. Shi, *RSC Adv.* **2017**, *7*, 33419; c) Y.-C. Wang, Z.-S. Sun, S.-Z. Wang, S.-Y. Wang, S.-X. Cai, X.-Y. Huang, K. Li, Z.-T. Chi, S.-D. Pan, W.-F. Xie, *J. Mater. Sci.* **2019**, *54*, 14055.

[14] a) H. Bi, Y. Shen, S. Zhao, P. Zhou, S. Gao, B. Cui, D. Wei, Y. Zhang, K. Wei, *Vacuum* **2020**, *172*, 109086; b) A. Khort, Y. Haiduk, I. Taratyn, D. Moskovskikh, K. Podbolotov, A. Usenka, N. Lapchuk, V. Pankov, *Sci. Rep.* **2023**, *13*, 7834; c) Y. Wang, L. Yao, L. Xu, W. Wu, W. Lin, C. Zheng, Y. Feng, X. Gao, *Sens. Actuators, B.* **2021**, *332*, 129497.

[15] S. M. Majhi, S. Navale, A. Mirzaei, H. W. Kim, S. S. Kim, *Inorg. Chem. Front.* **2023**, *10*, 3428.

[16] J. Yeo, S. Hong, D. Lee, N. Hotz, M.-T. Lee, C. P. Grigoropoulos, S. H. Ko, *PLoS One* **2012**, *7*, e42315.

[17] Y.-L. Zhang, Q.-D. Chen, H. Xia, H.-B. Sun, *Nano Today* **2010**, *5*, 435.

[18] a) R. Lakraimi, H. Abouchadi, M. T. Janan, A. Chehri, R. Saadane, *Materials* **2023**, *16*, 753; b) L. Papadakis, D. Chantzis, K. Salonitis, *The Int. J. Adv. Manufac. Technol.* **2018**, *95*, 1325; c) J. Chung, S. Ko, C. P. Grigoropoulos, N. R. Bieri, C. Dockendorf, D. Poulikakos, *J. Heat Transfer* **2005**, *127*, 724.

[19] S. Hong, J. Yeo, G. Kim, D. Kim, H. Lee, J. Kwon, H. Lee, P. Lee, S. H. Ko, *ACS Nano* **2013**, *7*, 5024.

[20] M. Al-Hashem, S. Akbar, P. Morris, *Sens. Actuators, B.* **2019**, *301*, 126845.

[21] B. Zhang, N. Bao, T. Wang, Y. Xu, Y. Dong, Y. Ni, P. Yu, Q. Wei, J. Wang, L. Guo, *J. Alloys Compd.* **2021**, *867*, 159076.

[22] S. S. Ham, H. Lee, *Polymers* **2018**, *12*, 959.

[23] C. E. Hoppe, M. Lazzari, I. Pardinas-Blanco, M. A. López-Quintela, *Langmuir* **2006**, *22*, 7027.

[24] a) D. Marrocchelli, S. R. Bishop, H. L. Tuller, B. Yildiz, *Adv. Funct. Mater.* **2012**, *22*, 1958; b) K. Bhattacharyya, B. Modak, C. Nayak, R. Nair, D. Bhattacharyya, S. Jha, A. Tripathi, *New J. Chem.* **2020**, *44*, 8559; c) W. Wei, Z. Wei, R. Li, Z. Li, R. Shi, S. Ouyang, Y. Qi, D. L. Philips, H. Yuan, *Nat. Commun.* **2022**, *13*, 3199.

[25] N. Rui, Z. Wang, K. Sun, J. Ye, Q. Ge, C.-j. Liu, *Appl. Catal., B.* **2017**, *218*, 488.

[26] a) Q. Hou, J. Buckeridge, T. Lazauskas, D. Mora-Fonz, A. A. Sokol, S. M. Woodley, C. R. A. Catlow, *J. Mater. Chem. C.* **2018**, *6*, 12386; b) J. Gan, X. Lu, J. Wu, S. Xie, T. Zhai, M. Yu, Z. Zhang, Y. Mao, S. C. I. Wang, Y. Shen, *Sci. Rep.* **2013**, *3*, 1021.

[27] C. Kranert, R. Schmidt-Grund, M. Grundmann, *Phys. Status Solidi (RRL)–Rapid Res. Lett.* **2014**, *8*, 554.

[28] S. Gohil, K. K. Iyer, P. Aswathi, S. Ghosh, E. Sampathkumaran, *J. Appl. Phys.* **2010**, *108*, 103517.

[29] M. Kaur, N. Jain, K. Sharma, S. Bhattacharya, M. Roy, A. Tyagi, S. Gupta, J. Yakhmi, *Sens. Actuators, B* **2008**, *133*, 456.

[30] A. Baszczuk, M. Jasiorski, M. Nyk, J. Hanuza, M. Mączka, W. Stręk, *J. Alloys Compd.* **2005**, *394*, 88.

[31] Z. Wang, Y. Zhou, D. Liu, R. Qi, C. Xia, M. Li, B. You, B. Y. Xia, *Angew. Chem.* **2022**, *134*, 202200552.

[32] D. Yoon, H. Moon, Y.-W. Son, J. S. Choi, B. H. Park, Y. H. Cha, Y. D. Kim, H. Cheong, *Phys. Rev. B—Condensed Matter and Mater. Phys.* **2009**, *80*, 125422.

[33] Z. Na, R. Yao, Q. Yan, X. Wang, X. Sun, *Appl. Surf. Sci.* **2020**, *513*, 145894.

[34] R. Daiyan, X. Lu, W. H. Saputera, Y. H. Ng, R. Amal, *ACS Sustainable Chem. Eng.* **2018**, *6*, 1670.

[35] M. Meng, L. Yang, X. Wu, Z. Gan, W. Pan, K. Liu, C. Li, N. Qin, J. Li, *J. Alloys Compd.* **2020**, *845*, 156311.

[36] N. Joshi, T. Hayasaka, Y. Liu, H. Liu, O. N. Oliveira, L. Lin, *Microchim. Acta.* **2018**, *185*, 213.

[37] a) D. Han, L. Zhai, F. Gu, Z. Wang, *Sens. Actuators, B.* **2018**, *262*, 655; b) H. Ma, L. Yu, X. Yuan, Y. Li, C. Li, M. Yin, X. Fan, *J. Alloys Compd.* **2019**, *782*, 1121.

[38] a) M.-W. Ahn, K.-S. Park, J.-H. Heo, J.-G. Park, D.-W. Kim, K. J. Choi, J.-H. Lee, S.-H. Hong, *Appl. Phys. Lett.* **2008**, *93*, 263103; b) B. Wang, Y. Wang, Y. Lei, S. Xie, N. Wu, Y. Gou, C. Han, Q. Shi, D. Fang, *J. Mater. Chem. C.* **2016**, *4*, 295.

[39] E. Halonen, T. Viiru, K. Ostman, A. L. Cabezas, M. Mantysalo, *IEEE Trans. Compon., Packag., Manuf. Technol.* **2012**, *3*, 350.

[40] S.-W. Fan, A. K. Srivastava, V. P. Dravid, *J. Appl. Phys.* **2009**, *95*, 142106.

[41] C. Zhang, X. Geng, J. Li, Y. Luo, P. Lu, *Sens. Actuators, B.* **2017**, *248*, 886.

[42] a) N. Liu, Y. Li, Y. Li, L. Cao, N. Nan, C. Li, L. Yu, *ACS Appl. Mater. Interfaces* **2021**, *13*, 14355; b) H. Zhu, Q. Li, Y. Ren, Q. Gao, J. Chen, N. Wang, J. Deng, X. Xing, *Small* **2018**, *14*, 1703974.

[43] S. Yang, H. Yin, Z. Wang, G. Lei, H. Xu, Z. Lan, H. Gu, *Front. Chem.* **2023**, *11*, 1174207.

[44] N. Wang, J.-X. Ye, J.-B. Sun, X.-F. Zhang, Z.-P. Deng, Y.-M. Xu, L.-H. Huo, S. Gao, *Sens. Actuators, B* **2022**, *361*, 131692.

[45] Y. Shen, X. Zhong, J. Zhang, T. Li, S. Zhao, B. Cui, D. Wei, Y. Zhang, K. Wei, *Appl. Surf. Sci.* **2019**, *498*, 143873.

[46] Y.-K. Lv, Y.-Y. Li, R.-H. Zhou, Y.-P. Pan, H.-C. Yao, Z.-J. Li, *ACS Appl. Mater. Interfaces* **2020**, *12*, 34245.

[47] J. Berkowitz, W. Chupka, D. Gutman, *J. Chem. Phys.* **1971**, *55*, 2733.

[48] A. Posada-Borbon, H. Grönbeck, *Phys. Chem. Chem. Phys.* **2020**, *22*, 16193.

[49] G. Henkelman, B. P. Uberuaga, H. Jónsson, *J. Chem. Phys.* **2000**, *113*, 9901.

[50] B. Zhang, R. Shi, W. Duan, Z. Luo, Z.-y. Lu, S. Cui, *RSC Adv.* **2017**, *7*, 33883.

[51] a) Y. Liu, J. Li, W. Hou, Q. Zhou, W. Zeng, *J. Mater. Res. Technol.* **2022**, *18*, 4236; b) Y. Ou, G. Zhu, P. Liu, Y. Jia, L. Zhu, J. Nie, S. Zhang, W. Zhang, J. Gao, H. Lu, *ACS Sens.* **2022**, *7*, 1201.

[52] D. Xue, Y. Wang, Z. Zhang, J. Cao, *Sens. Actuators, A.* **2020**, *305*, 111944.

[53] S.-b. Liu, J. Li, Y. Zhang, X. Xu, Z. Chen, *J. Mol. Struct.: THEOCHEM* **2008**, *866*, 75.